Theor. Comput. Fluid Dyn. (2024) 38:937–951
https://doi.org/10.1007/s00162-024-00715-z

ORIGINAL ARTICLE

Eduardo Martini · Clement Caillaud · Guillaume Lehnasch · Peter Jordan · Oliver Schmidt

Perturbation amplification near the stagnation point of blunt bodies

Received: 1 December 2023 / Accepted: 16 July 2024 / Published online: 16 September 2024

Abstract Different transition to turbulence routes for the flow around blunt bodies are possible. Non-modal amplification of perturbations via the lift-up effect has recently been explored to explain transition near the stagnation point in axisymmetric bodies. However, only perturbations already present in the boundary layer can be amplified, and the mechanisms by which free-stream perturbations enter the boundary layer have not yet been fully explored. In this study, we present an investigation of how disturbances enter the boundary layer via the stagnation point. This linear mechanism is expected to dominate over non-linear mechanisms previously identified on the formation of boundary layer perturbations at low turbulence intensity levels. A parametric investigation is presented, revealing trends with Reynolds and Mach numbers.

Keywords Flow receptivity · Resolvent analysis · Linear flow analysis

1 Introduction

Turbulent boundary layers enhance viscous drag and higher heat flux to the bodies about which they develop. Predicting where a boundary layer will transition from a laminar to a turbulent state is necessary to predict aerodynamic performance. In supersonic flight, the transition point is also a key design parameter as turbulent boundary layers exchange more heat with the surface and thus require more robust thermal shielding.

Communicated by Stefania Cherubini.

E. Martini (✉) · C. Caillaud · G. Lehnasch · P. Jordan
Département Fluides, Thermique, Combustion, Institut Pprime, CNRS-Universitè de Poitiers-ENSMA, 1 Bd Marie et Pierre Curie, 86962 Futuroscope Chasseneuil, la Vienne, France
E-mail: eduardo.martini@ensma.fr

G. Lehnasch
E-mail: Guillaume.Lehnasch@ensma.fr

P.Jordan
E-mail: peter.jordan@univ-poitiers.fr

E. Martini · C. Caillaud
Commissariat à l'Énergie Atomique, CESTA, 15 Avenue des Sablières, 331163 Le Barp, la Vienne, France
E-mail: clement.caillaud@cea.fr

O. Schmidt
Departament of Mechanical and Aerospace Engineering, University of California San Diego, 9500 Gilman Drive, La Jolla, California 92093-0411, USA
E-mail: oschmidt@ucsd.edu

Earlier work issued from local stability theory describes several paths for transition in wall-bounded flows [24]. In scenarios where perturbations present in the free stream or due to surface roughness are small, the mechanism that leads to transition is typically modal, i.e., unstable modes in the boundary layer grow exponentially and eventually trigger transition. By-pass transition is another possible mechanism when small-but-finite perturbations are present. The mechanism is characterized by a non-modal amplification of these perturbations, which may then reach significant amplitudes and lead to flow transition. As only perturbations within the boundary layer can lead to its transition, it is necessary to understand their origin, i.e., how they enter or are generated within the boundary layer.

Perturbations can be created within a boundary layer, e.g., by roughness elements or be excited by external disturbances. Acoustic waves can excite Tollmien-Schlichting (TS) waves at points of curvature discontinuity Goldstein [9]. Free-stream disturbances can excite vortical modes in the boundary layer via non-linear interactions, as studied by Brandt et al [2]. In this study, the non-linear mechanism was dominant at moderate to large free-stream turbulence intensities, while pre-existing boundary layer structures' amplification was more relevant at lower turbulence intensities and larger integral wavelengths. The study suggests that such vortical structures may penetrate the boundary layer at the leading edge, although this mechanism was not investigated. Thus, such a linear mechanism is expected to dominate receptivity at low turbulent intensities.

For higher Mach numbers, different receptivity mechanisms may be observed. For example, in supersonic flows, there are regions for which Mack waves [20] have wavelengths matching that of acoustic waves, and can thus be directly excited by them [34].

Numerical studies on the leading-edge receptivity typically use smooth surfaces, i.e., with continuous curvatures, to prevent the results from being contaminated by the length-conversion mechanism identified by Goldstein [9]. Leading edges shaped as super-ellipses [3,15,33,37] and parabolic bodies [11] are among the examples studied. Haddad and Corke [11] have identified that the receptivity of TS waves decreases with Reynolds number on a paraboloid body, i.e., with increasing bluntness. This result contrasts with a more recent review on thick flat plates with curved leading edges [33]. The reason for this discrepancy is unclear, but they may be related to different flow regimes. The study of Haddad and Corke [11] may only be valid around the stagnation point, and, while the super-ellipse studied by Shahriari et al [33] is formally smooth, the surrounding flow can exhibit strong gradients, whose contribution to the receptivity mechanism is unclear. As a favorable pressure gradient stabilizes TS waves near the stagnation point, TS waves amplitudes are typically small around it. However, they can be amplified downstream, where the pressure gradient asymptotically vanishes. Mack waves exhibit a similar behavior in supersonic flows due to the low velocities near the stagnation point.

Nevertheless, there are circumstances where transition is observed close to the leading edge, e.g., in hypersonic blunt bodies [27]. For these configurations, different mechanisms have been proposed. Entropy layer perturbations can be amplified and penetrate the boundary layer when the entropy layer is swallowed or be imprinted on it via non-linear mechanisms upstream of the swallowing point [7,28]. Another transition route is the onset of leading-edge modal instabilities [16,17]. However, the former can only lead to transition after the ingestion point, which occurs further downstream than the observed transition point, and the latter is only active in the presence of a crossflow. When no crossflow is present, such modal mechanisms cannot explain these transitions, motivating the study of non-modal mechanisms in the nose region [27].

The lift-up is a non-modal mechanism that is ubiquitous in shear flow. It consists of streamwise vortices that move flow from regions with higher velocities to regions with lower velocities and vice versa, creating alternating regions of fast and slow streamwise velocities, known as streaks. Under a parallel flow assumption, linear stability theory predicts amplitude amplification to scale with Re for spanwise wavelengths of the order of two boundary layer thickness in both compressible and incompressible flows [1,12,18,29]. Large perturbation amplification is also observed in spatially evolving boundary layers [14,23,27,35].

The vorticity dynamics entering the boundary layer via the leading edge have received less attention. Obrist and Schmid [26] studied the problem using Hiemenz's self-similar flow model, Mack and Schmid [19] and Meneghello et al [22] studied swept flow over a parabolic body and a wing leading edge. However, there are virtually no studies investigating the problem of unswept flows.

In this study, we present a systematic investigation of non-modal mechanisms at the leading edge using a paraboloid body as a flow model. We systematically investigate the role of bluntness and compressibility to provide a cartography of the phenomena.

The paper is structured as follows. Section 2 presents the flow around the paraboloid body. Section 3 presents the numerical methods used in the linear stability analysis. Section 4 presents a study of the perturbation amplification mechanisms near the stagnation point using the resolvent framework. Section 5 expands the results to investigate compressible flows, with Mach number up to 1.2. Section 6 presents the final conclusions.

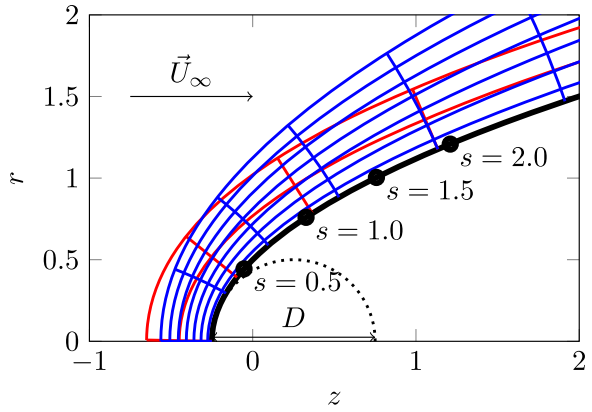

Fig. 1 Illustration of the geometry and the coordinate systems used. Red and blue lines illustrate parabolic and body-fitted coordinates, respectively. The thick black line indicates the body surface. The dotted circle is tangent to the leading edge. The arrow indicates the freestream velocity. Points with a distance of multiples of 0.5 length units from the stagnation point are shown for reference

2 Paraboloid body

The body surface studied is given by

$$x = (z^2 + y^2) - 1/4, \tag{1}$$

with the free-stream flow moving towards $+z$. The flow parameters are made non-dimensional using the freestream density, viscosity, and velocity. As the reference length, we use the curvature diameter of the leading edge.

Three coordinate systems are considered. All computations use cylindrical coordinates, which will be detailed later. Paraboloid coordinates (σ, τ) are used and defined in Sect. 2.1 to obtain an inviscid potential flow analytically. Finally, body-fitted coordinates (s, d) are defined as the distance from the leading edge along the body surface and the distance from the body surface. The latter are used for visualization and post-processing only. Figure 1 illustrates the problem and coordinate systems used.

2.1 Inviscid and incompressible flow

The potential flow around the body is obtained analytically using parabolic coordinates, (σ, τ, ϕ), defined as,

$$z + \mathrm{i}r = (\sigma + \mathrm{i}\tau)^2, \qquad r = \sqrt{(x^2 + y^2)}, \qquad \phi = \tan^{-1}(y/x). \tag{2}$$

The body surface is located at $\sigma = \sigma_0 = -1/2$.

The flow potential function, ψ, satisfies the Laplace equation,

$$\nabla^2_{\sigma,\tau,\phi}\psi = \frac{1}{\sigma}\frac{d}{d\sigma}\left(\sigma\frac{d\psi}{d\sigma}\right) + \frac{1}{\tau}\frac{d}{d\tau}\left(\tau\frac{d\psi}{d\tau}\right) + \frac{d^2\psi}{d\phi^2}, \tag{3}$$

with, as boundary conditions, no penetration at the body surface and the convergence to the free-stream conditions far from the body. These conditions read

$$\frac{d\psi}{d\sigma} = 0, \qquad \text{for } \sigma = \sigma_0 \quad \text{and} \tag{4}$$

$$\psi = z = (\sigma^2 - \tau^2), \qquad \text{for } \sigma \to \infty. \tag{5}$$

The solution to (3) under (4) and (5) is given by

$$\psi = \sigma^2 - \tau^2 + 2\sigma_0^2 \log(\sigma). \tag{6}$$

Table 1 List of Reynolds numbers investigated for the incompressible case

Reynolds numbers									
100	500	1000	5000	30000	60,000	120,000	180,000	240,000	300,000

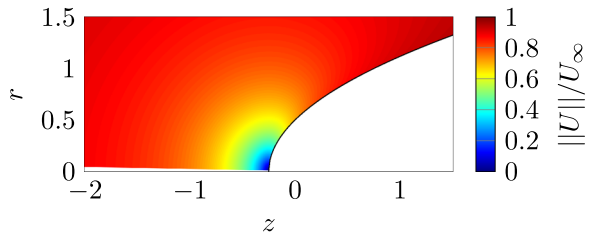

Fig. 2 Potential flow around the paraboloid body

The velocity field is then recovered as

$$U_z = \frac{\partial \psi}{\partial x} = \frac{\partial \psi}{\partial \sigma}\frac{\partial \sigma}{\partial x} + \frac{\partial \psi}{\partial \sigma}\frac{\partial \tau}{\partial x}, \tag{7}$$

$$U_r = \frac{\partial \psi}{\partial y} = \frac{\partial \psi}{\partial \sigma}\frac{\partial \sigma}{\partial y} + \frac{\partial \psi}{\partial \sigma}\frac{\partial \tau}{\partial y}. \tag{8}$$

The potential flow is illustrated in Fig. 2, where the stagnation point and subsequent flow reacceleration are observed.

2.2 Viscous incompressible flow

A 2D axisymmetric model was used to obtain base flows for the viscous problem. No-slip boundary conditions were applied at the body surface; Neumann boundary conditions for the velocity (open boundary condition) were used on the right-most edge of the domain, and the potential flow was imposed on the left-most edge as an inflow condition, reducing the domain size required to converge the solutions. The problem was time-marched using the open-source code Nek5000 [8] until the norm of the velocity time derivative became smaller than 10^{-8}.

This process was repeated for several Reynolds numbers between 100 and 300,000, listed in Table 1. The domain size was adapted for each Reynolds number: larger domains were used at lower Reynolds numbers to minimize blockage effects, and smaller domains at larger Reynolds numbers to avoid unnecessary computational costs. The Reynolds-number range was chosen to reach values sufficiently high for an asymptotic trend to be observed and lower values where the behavior deviates from the trend.

Figure 3 illustrates the base flows obtained. For $Re \gtrapprox 5000$, the flow is qualitatively similar to the potential flow shown in Fig. 2 but with the formation of a boundary layer around the body surface. The base flows are similar but with thinner boundary layers for higher Reynolds numbers.

Figure 4b shows the wall-tangential velocity profile for $s = 1$, i.e., at unit distance from the stagnation point. A thicker boundary layer is formed for lower Reynolds numbers, and the flow at its edge has larger velocities than the potential flow, compensating for the loss of mass flow closer to the wall. This effect reduces with Re and is negligible for $Re > 5000$. As expected, the flow converges to the potential solution away from the wall for higher Reynolds numbers.

The decreasing velocity magnitude with the potential flow's wall distance and the wall's no-slip boundary condition creates a velocity maximum at a distance d_{max} from the wall. We thus define the boundary layer thickness for the problem as,

$$\delta^*(s) = \int_0^{d_{max}} \left(\frac{U_{\parallel,\mathrm{pot}}(s,d) - U_\parallel(s,d)}{U_{\parallel,\mathrm{pot}}(s,0)} \right) \mathrm{d}d. \tag{9}$$

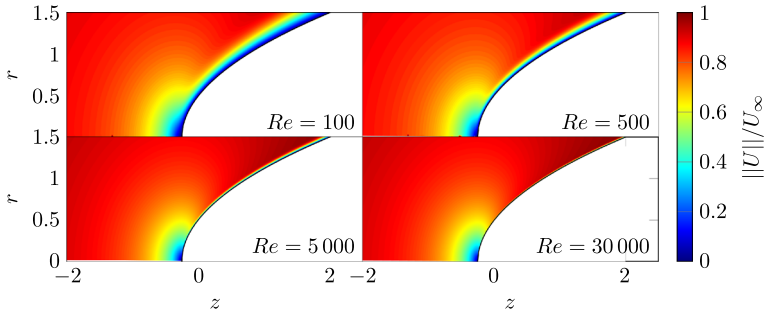

Fig. 3 Velocity magnitude of the baseflow for different Reynolds numbers. For clearness, only selected cases are shown

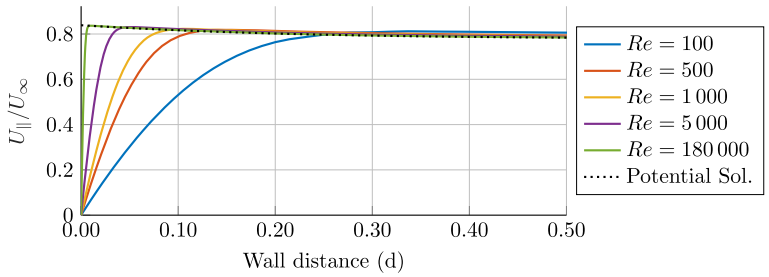

(a) Wall-tangent velocity ($U_\parallel$) profile at the wall position $x = 0.3$, $s \approx 0.95$.

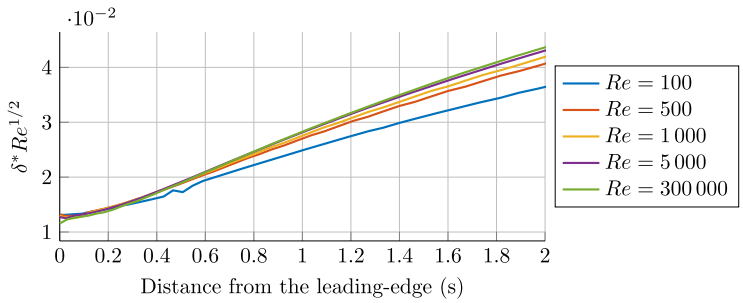

(b) Boundary layer displacement thickness.

Fig. 4 Boundary layer profile and thickness for the flow around the paraboloid body

where $U_\parallel$ indicates velocity component parallel to the wall, and $U_{\parallel,\text{pot}}$ corresponds to the potential solution. Note that $U_{\parallel,pot}(s, 0) = 1$ for a flat plate, and (9) recovers the classical definition of the displacement thickness.

Figure 4b shows the evolution of the boundary layer profile. Near the stagnation point, the boundary layer is formed with a thickness that scales with $Re^{-1/2}$, as predicted when the region is modeled by a Homann flow [13,39]. Downstream, the boundary layer evolution reaches the asymptotic limit, scaling with $Re^{-1/2}$ for $Re \gtrapprox 5000$.

3 Numerical method

We will perform resolvent analysis on a 2D axisymmetric flow to study the perturbation amplification. The numerical method is derived from that used by Schmidt et al [32] and Schmidt and Rist [30,31], with the code adapted to use curvilinear coordinates. We refer readers to the original document for details of the code, describing only its main features next.

3.1 Resolvent analysis

The discretized linearized Navier–Stokes equations written in input–output form in the frequency domain

$$\begin{aligned}(-\mathrm{i}\omega - \mathbf{A})\hat{\boldsymbol{u}}(\omega) &= \mathbf{B}\hat{\boldsymbol{f}}(\omega),\\ \hat{\boldsymbol{y}}(\omega) &= \mathbf{C}\hat{\boldsymbol{u}}(\omega),\end{aligned} \tag{10}$$

where $\mathbf{A}$ is the discretized representation of linearized Navier-Stokes operator around a fixed point, $\mathbf{B}$ and $\mathbf{C}$ are matrices introduced to limit input (forcing) and output (responses) spaces. E.g., these can be used to limit forcings and responses to regions near the boundary layer, avoiding the contamination of the results by free-stream modes [25]. The forcing and response vectors are, respectively, $\hat{\boldsymbol{f}} = [\hat{f}_\rho, \hat{f}_{u_z}, \hat{f}_{u_r}, \hat{f}_{u_\theta}, \hat{f}_T]^T$, and $\hat{\boldsymbol{u}} = [\hat{\rho}, \hat{u}_z, \hat{u}_r, \hat{u}_\theta, \hat{T}]^T$.

A direct relation between input and the output is obtained as

$$\hat{\boldsymbol{y}}(\omega) = \mathbf{R}(\omega)\hat{\boldsymbol{f}}(\omega), \tag{11}$$

where

$$\mathbf{R}(\omega) = \mathbf{C}(-\mathrm{i}\omega - \mathbf{A})^{-1}\mathbf{B}, \tag{12}$$

is the resolvent operator [29].

A forcing term is said to be optimal if it maximizes the Rayleigh ratio,

$$\sigma(\omega) = \frac{\left\|\hat{\boldsymbol{y}}(\omega)\right\|_{\mathbf{W}_y}}{\left\|\hat{\boldsymbol{f}}(\omega)\right\|_{\mathbf{W}_f}} = \frac{\left\|\mathbf{R}(\omega)\hat{\boldsymbol{f}}(\omega)\right\|_{\mathbf{W}_y}}{\left\|\hat{\boldsymbol{f}}(\omega)\right\|_{\mathbf{W}_f}}, \tag{13}$$

and can be obtained from a singular value decomposition (SVD) of the weighted resolvent operator $\mathbf{R}'(\omega) = \mathbf{W}_y^{-1/2}\mathbf{R}(\omega)\mathbf{W}_f^{1/2}$, where $\mathbf{W}_{y/f}$ are the weight matrices for responses and forcings, respectively [32]. The ratio σ measures the gains in terms of the modes norm, while energy gains are given by σ^2. This study's weight matrices include integration quadrature weights and an energy norm for compressible flows. Two different energy norms are used: kinetic,

$$\|\hat{\boldsymbol{y}}\|^2 = \int \overline{\rho}\left(|\hat{u}_z|^2 + |\hat{u}_\theta|^2 + |\hat{u}_r|^2\right)\mathrm{d}V \tag{14}$$

and compressible [4,12],

$$\|\hat{\boldsymbol{y}}\|^2 = \int \left(\frac{\overline{T}}{\overline{\rho}\gamma Ma^2}|\hat{\rho}|^2 + \overline{\rho}|\hat{u}_z|^2 + \overline{\rho}|\hat{u}_\theta|^2 + \overline{\rho}|\hat{u}_r|^2\frac{\overline{\rho}}{\overline{T}\gamma(\gamma-1)Ma^2}|\hat{T}|^2\right)dV. \tag{15}$$

norms, where the overline variables refer to the baseflow fields, γ is the adiabatic coefficient, and M is the Mach number.

Different strategies to compute the SVD can be used. For problems with only one inhomogeneous direction, $\mathbf{R}(\omega)$ is a small matrix, and standard tools are effective in obtaining the decomposition. On the other hand, for three-dimensional problems, methods based on time-marching schemes are typically used [6,10,21,23]. For two-dimensional problems where one direction is homogeneous, effective approaches use sparse matrices to represent $\mathbf{A}$, solving the linear system (10) to obtain the action of the resolvent operator on a vector. The latter approach is used in this work.

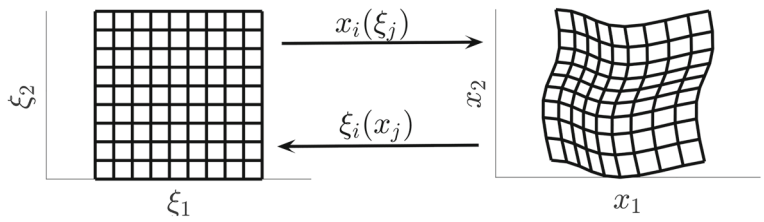

Fig. 5 Illustration of mapping between the computational (ξ_i) and physical (x_i) meshes

3.2 Curvilinear coordinates

In order to construct the linearized operator, derivative matrices for the domain are required. These matrices were constructed by mapping a square domain (described with coordinates ξ_i), for which derivatives are computed using standard finite differences, into the desired domain (described with coordinates x_i), as illustrated in Fig. 5. Centered and uncentered fourth-order finite-difference schemes were used on the bulk of the domain and at the domain boundaries, respectively.

In general, the mapping between ξ_i and x_i is given implicitly: for a given node in the original mesh, $x_i(\xi_j)$ corresponds to the coordinate of the same node on the mapped domain. The inverse function, $\xi_i(x_j)$, is likewise available. Henceforth, we will refer to $x_i(\xi_j)$ simply as the mapping, and to $\xi_i(x_j)$ as the inverse mapping.

The derivative of a function g is written using the chain rule as

$$\partial_{x_i} g = J_{ij}\partial_{\xi_j} g, \tag{16}$$

where $J_{ij} = \frac{\partial \xi_i}{\partial x_j}$ are (i, j) entries of $\mathbf{J}$, the Jacobian of the function that maps (x_1, x_2) to (ξ_1, ξ_2), i.e., the inverse of the mapping function. As only differentiation matrices w.r.t. ξ_i are a priori available, we construct first $J_{ij}^{-1} = \frac{\partial x_j}{\partial \xi_i}$. We then obtain $\mathbf{J}$ by inverting $\mathbf{J}^{-1}$.

Equation (16) can be iterated to obtain second-order derivatives. However, this increases the effective stencil of the method, which increases the cost of solving the resulting linear systems. To avoid larger stencils, we describe the second derivative as

$$\begin{aligned}\partial_{x_i}\partial_{x_j} g &= \partial_{x_i}\left(J_{jq}\partial_{\xi_p} g\right)\\ &= \left(\partial_{x_i} J_{jp}\right)\partial_{\xi_p} g + J_{jp}^{-1}\left(\partial_{x_i}\partial_{\xi_p} g\right)\\ &= \left(\partial_{x_i} J_{jp}\right)\partial_{\xi_p} g + J_{jp}^{-1} J_{iq}\partial_{\xi_q}\partial_{\xi_j} g,\end{aligned} \tag{17}$$

computing $\left(\partial_{x_i} J_{ij}\right)$ via the matrix identity

$$\partial_{x_i}\mathbf{J} = \mathbf{J}\left(\partial_{x_i}\mathbf{J}^{-1}\right)\mathbf{J}. \tag{18}$$

Finally, the term $\partial_{x_i}\mathbf{J}^{-1}$, reads

$$\partial_{x_i} J_{lm}^{-1} = J_{ji}^{-1}\partial_{\xi_i} J_{lm}^{-1} = J_{ij}^{-1}\frac{\partial^2 x_l}{\partial\xi_i\partial\xi_m}. \tag{19}$$

With this approach, the stencil size in the physical domain (x_i) has the same size as that of the computational domain (ξ_i).

4 Receptivity

We start by investigating the receptivity of the $Re = 30{,}000$ baseflow. A Cartesian grid with 100×100 points was mapped around the body, with nodes clustered near the surface to resolve the boundary layer. Dirichlet boundary conditions were used on all boundaries. A sponge zone was used to avoid spurious reflection near the inflow/outflow boundaries. The convergence of all the results presented was checked, and variations less than 1% when using a finer mesh were observed.

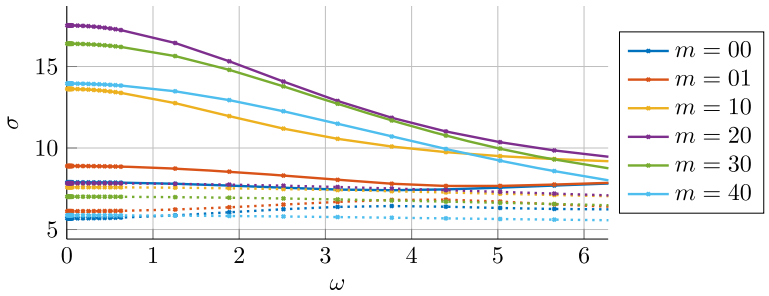

Fig. 6 Gain variation with frequency for the $Re = 30{,}000$ flow. Leading/suboptimal gains in solid/dashed lines for different azimuthal numbers m

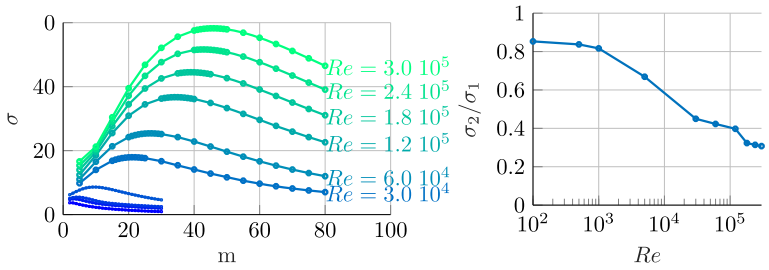

(a) Leading gains (b) Gain separation

Fig. 7 Leading gains (**a**) and suboptimal gains for the dominant azimuthal number (**b**). The unlabelled lines in **a** correspond to $Re = 100$, 500, 1000, and 5000, from the bottom up

As will be shown next, the spatial support of the forcing/response modes can extend far up/downstream. Fully capturing these structures requires a large domain, making the analyses too costly. Since the study aims to investigate how free-stream disturbances penetrate the boundary layer, the downstream domain was limited to $s \lessapprox 2$. The domain upstream was limited to $z \gtrapprox -6$. Down/upstream of these limits, a sponge zone is used to dampen perturbations before the boundary of the computation domain.

Figure 6 shows the frequency dependency of the leading gains for different azimuthal wavenumbers. The largest gain is found for $\omega = 0$, which suggests that the lift-up mechanism is dominant around the leading edge. Henceforth, we concentrate the study on gains associated with zero-frequency disturbances. Note, however, that this analysis is representative of low-frequency dynamics, as illustrated in Fig. 6.

Although zero-frequency disturbances can be considered as a new baseflow, the results presented are representative of low-frequency perturbations, i.e., $\omega \lesssim 0.1$. They also indicate the sensitivity of the baseflow to steady disturbances, i.e., how much the baseflow is modified with a given (small) change in the forcing.

We next perform a systematic parametric investigation, computing gains at $\omega = 0$ for different Reynolds and azimuthal numbers. The numerical grid was adapted for each scenario as the boundary layer thickness varied considerably between the different cases. The Cartesian grid size between 75×75 and 100×175 gridpoints were used, with the last number corresponding to the wall-normal direction near the body surface, to discretize the boundary layer. The results are presented in Fig. 7a, which shows that both the maximum gain and the corresponding azimuthal wavenumber increase with Re. Figure 7b shows that the difference between the leading and the suboptimal gains tends to also increase with Re, which points towards an increasing selectivity of disturbances.

To illustrate the forcing and response modes, Fig. 8 shows their support for the highest gain observed for $Re = 5000$ and $m = 9$. Although this case has a moderate gain, the relatively thick boundary layer facilitates visualization of the flow features. In this, and all other similar figures to be presented, the modes were normalized such that the maximum absolute value of a response/forcing component is equal to one. Note that, as observed for the lift-up mechanisms in flat plates, the azimuthal and streamwise velocity components are out-of-phase, and thus, in Fig. 8, the θ components are small. Figure 9 shows a 3D visualization of the flow, in which the phase difference between $\hat{u}_\theta$ and $\hat{u}_x$ can be observed.

The modes for higher Reynolds numbers are qualitatively similar. Both forcing and response modes are concentrated in the z and r components. The forcing mode excites vorticity perturbations upstream of the leading edge. Over the surface, the response mode is mostly dominated by the streamwise velocity component.

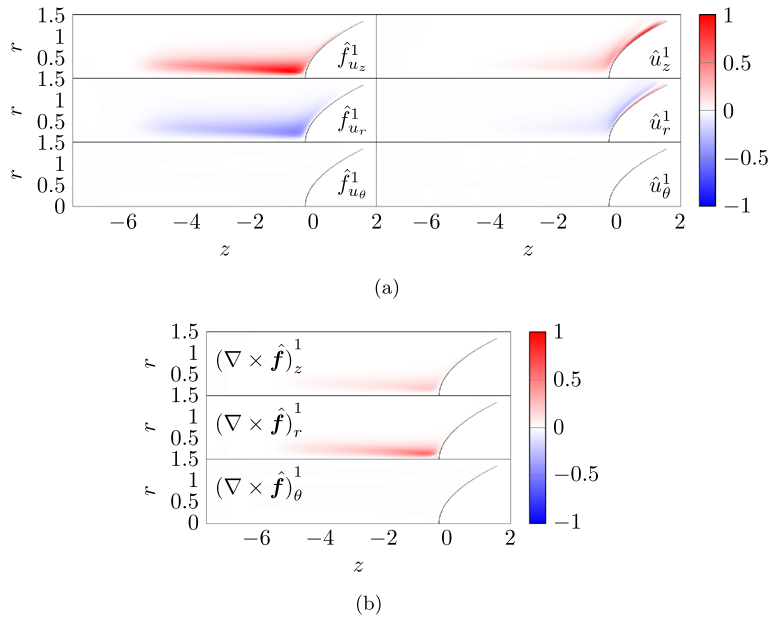

Fig. 8 Leading forcing and response modes (**a**) and the curl of the forcing mode (**b**) for $Re = 5000$ and $m = 9$. The modes are normalized by their largest absolute value. Color scales indicate the real part of the modes

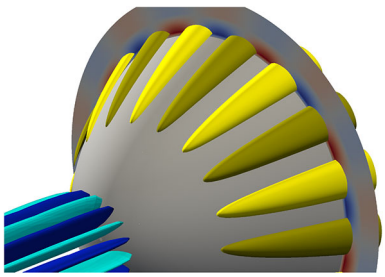

Fig. 9 Three-dimensional visualization of Fig. 8. Isocontours of the u component of forcing and response modes are shown in blue/yellow, with light and dark colors representing isovalues of -0.5 and 0.5, respectively. The red and blue color scale shows the azimuthal component of the response mode at the plane normal to the axis of symmetry, saturated at a value of ± 0.4

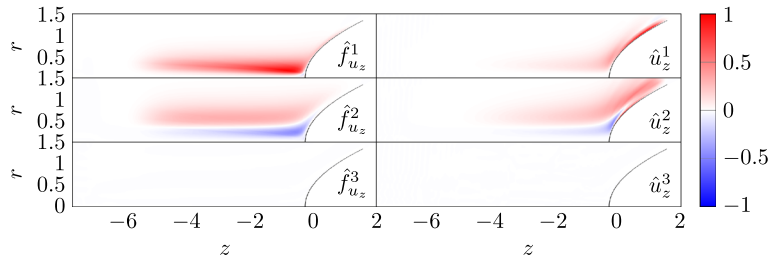

Fig. 10 Leading and suboptimal forcing and response modes. Results for $Re = 5000$ and $m = 9$. The modes are normalized by their largest absolute value. Color scales indicate the real part of the modes

These observations suggest that the dominant mechanism at play consists of free-stream streamwise vortices penetrating the boundary layer at the stagnation point and creating streamwise streaks via the lift-up mechanism. The r component of the vorticity creates streaks near the stagnation point, and the z component acts further downstream, where the flow becomes more aligned with the z axis. Although for the low Re case discussed here, the forcing mode has support over a large part of the body, as will be shown later, this support is increasingly concentrated near the symmetry axis, suggesting that the resulting perturbations are convected into the boundary layer via the stagnation point.

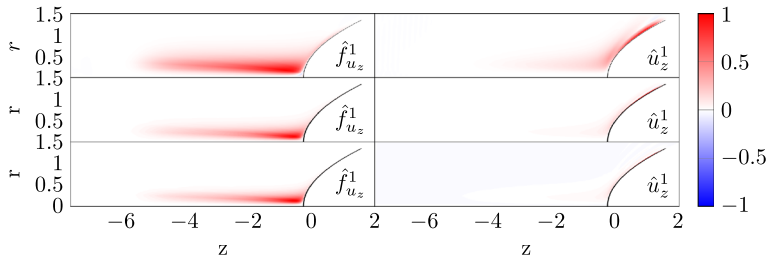

Fig. 11 Spatial support of the leading forcing and response modes. From top to bottom, results for $Re = 5000$, 30,000, and 60,000, with azimuthal wave number corresponding to the highest gain for each Re. The modes are normalized by their largest absolute value. Color scales indicate the real part of the modes

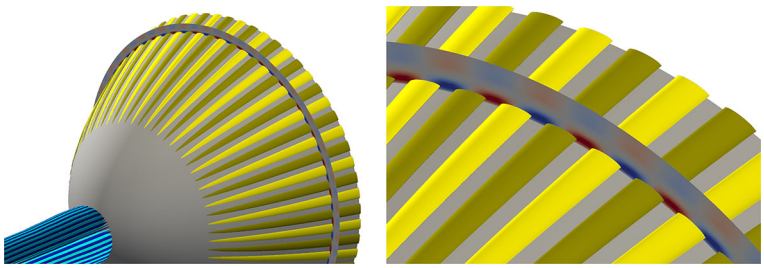

Fig. 12 Three-dimensional visualization of the leading response mode for $Re = 120{,}000$ ($m = 39$). Contours are equivalent to Fig. 9, but here isocontours are saturated at ± 0.1

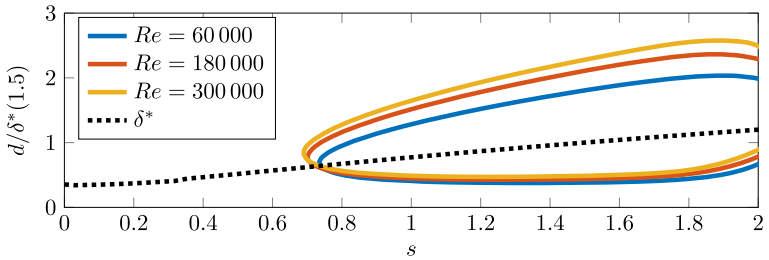

Fig. 13 Isocontours of half of the leading response mode peak value for different Reynolds numbers. The displacement thickness for $Re = 300{,}000$ is shown for reference

The spatial support of the forcing modes extends upstream with the Reynolds numbers, and thus, resolving it requires large domains. We limit the upstream domain, as it captures the relevant physical mechanism.

Figure 10 compares the support for the optimal and suboptimal force and response modes. The suboptimal modes exhibit nodes in the radial direction for both the forcing and response modes, similar to the streak force and response modes in jets [38]. The sub-optimal modes for all cases studied here presented a similar structure.

The evolution of the modes with Reynolds number is shown in Fig. 11. As Re increases, the boundary layer's initial size decreases; thus, a smaller region of the flow around the centerline is convected within it. The forcing modes are concentrated in these regions to exploit the lift-up mechanism in the boundary layer. Figure 12 shows a 3D visualization of the leading mode for $Re = 120{,}000$.

Figure 13 shows the contour of the response modes scaled by the boundary layer thickness using the wall-fitted coordinates (s, d), previously shown in Fig. 1. The modes are distributed around the boundary layer displacement thickness. A slight wall-normal displacement of the modes is observed for the highest Re numbers. Whether this trend persists for higher Reynolds numbers or its implication is unclear.

Figure 14 shows the trends associated with the optimal gains, σ_{opt}, and the corresponding azimuthal wavenumbers, m_{opt}, with Re. For $Re \geq 30{,}000$, σ_{opt} follows a $Re^{1/2}$ scaling, while m_{opt} scales with $Re^{0.34}$. We believe that the trend for the optimal m is due to the axisymmetric geometry: a given value of m implies a different "spanwise wavelength" $(2\pi r/m)$ for different positions at the body. Different azimuthal numbers are optimally amplified locally at each position as the boundary layer thickness increases with the distance to the stagnation point. A trade-off between different amplification rates at different positions may be responsible for the observed trend.

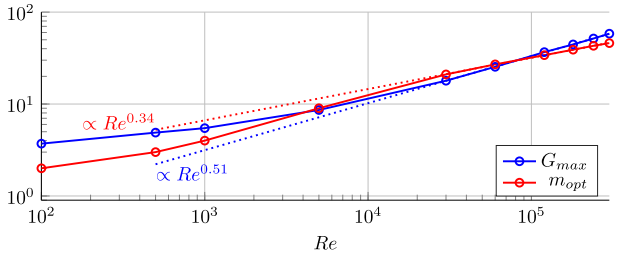

Fig. 14 Reynolds number scaling of the maximum gain and the corresponding azimuthal number. Dotted lines show a linear fit for $Re \geq 3 \times 10^4$

5 Compressibility effects

Having explored the receptivity of the incompressible paraboloid flow, we now assess the effect of compressibility for increasing Mach numbers. We investigate Mach numbers 0.3, 0.6, 0.9, and 1.2, and fix the Reynolds number to the value of 30,000, for which the asymptotic trend observed in Fig. 14 is reached. In this study, we consider ideal gases, with an adiabatic exponent $\gamma = 1.4$ and the viscosity dependency on the temperature given by Sutherland's empirical formula

$$\mu(T) = \mu_{\text{ref}} T^{3/2} \frac{1 + T_s}{T + T_s} \tag{20}$$

where $\mu_{\text{ref}}(T_{\text{ref}} = 280\text{K}) = 1.735 \times 10^{-5}$ kg/ms and $T_s = 110.4\text{K}/T_{\text{ref}}$ for standard air, is used to obtain the dynamic viscosity from the temperature. Finally, thermal conductivity is obtained by assuming a constant Prandl number, $Pr = 0.7$.

Baseflows are obtained using the software StarCCM+. Freestream values and adiabatic walls are used as boundary conditions. Baseflows were converged until the residuals were smaller than 10^{-8}. The resulting baseflows are illustrated in Fig. 15.

As mentioned by Edgington-Mitchell et al [5], the effect of shocks in linear stability analysis still carries some uncertainties with it. For this reason, we limited the analysis to weak shocks, Mach 1.2, and smoothed the shock discontinuities, as shown in Fig. 15. We also used a finer mesh (200×200 grid points) than in the previous analysis.

We considered two cases, one using a kinetic energy norm (14), i.e., restricting the force- and response-mode norm to the velocity components, and another considering temperature and density variations, using a compressible energy norm (15). While it can be argued to be more generic, it has been argued that velocity perturbations are more likely to trigger flow transition. We thus choose to study both.

Figure 16 shows the gains associated with flows with increasing Mach numbers. Results are similar to those of the incompressible flow, with a monotonic increase in value with Mach number, which is consistent with the results presented by Tumin and Reshotko [36]. The reduction of the optimal spanwise wavenumber shown in their study is also observed in Fig. 16. The trend of the peak gain for each condition is summarized in Fig. 17.

Polynomial and exponential curves were fitted to the data. The results suggest an exponential trend of the leading gain with Mach number, shown in 17. We emphasize that this result should be considered preliminary, both due to the small number of points available (4 points for 3 parameters), and due to the limited mach number range considered. Nevertheless, this points to a strong amplification effect for higher Mach numbers.

The support of the optimal forcing and response modes are shown in Fig. 18. The support of the forcing terms of the momentum equations remains qualitatively similar, and the shock, located around $z \approx 2$, does not seem to affect these terms. Extra forcing terms for the continuity and energy equations appear, showing a transition for the regions before and after the shock. Again, the flow responses are qualitatively similar, but with density and temperature fluctuations becoming more pronounced for higher Mach numbers.

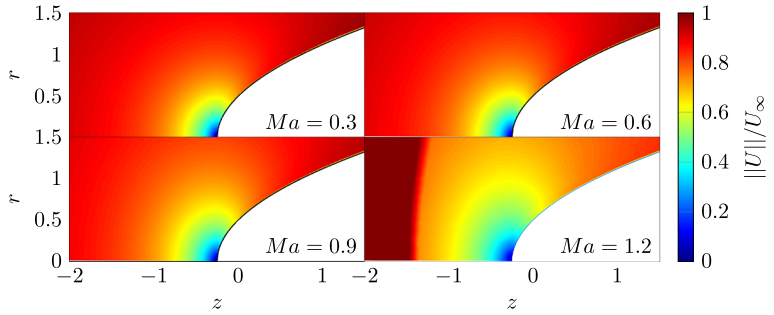

Fig. 15 Illustration of the velocity profiles for different Mach numbers for $Re = 3 \times 10^4$

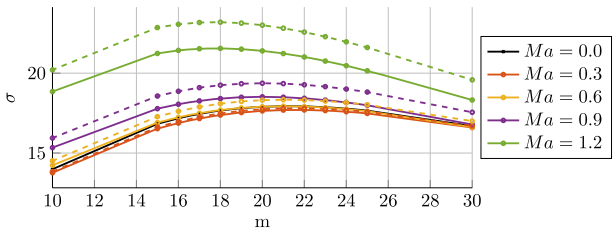

Fig. 16 Gains for the leading zero frequency mode for different Mach numbers. Solid lines indicate results where forcing and responses are restricted to the momentum equations and velocity components. Dashed lines consider temperature and density fluctuations

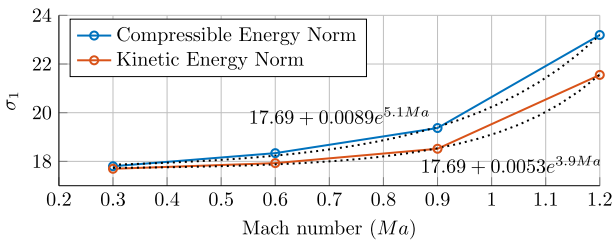

Fig. 17 Optimal gain trend with Mach number

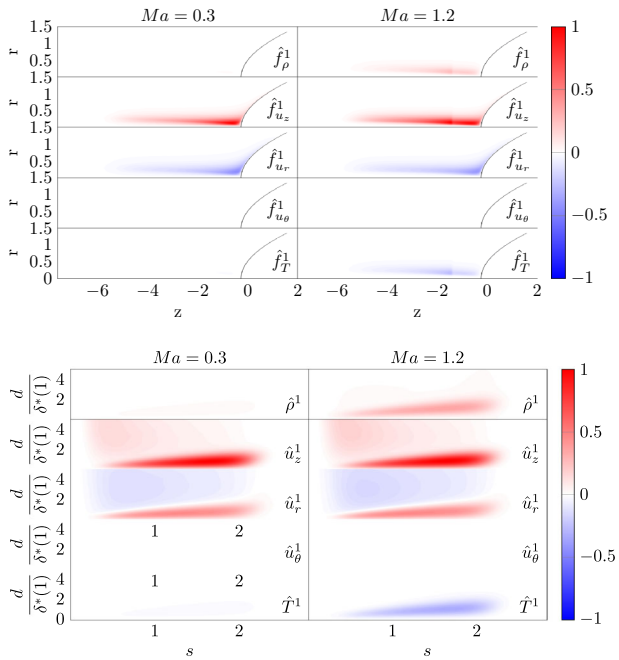

Fig. 18 Forcing and response modes for $m = 21$ modes for the compressible flow cases. Color scales indicate the real part of the modes

6 Conclusions

We have presented a parametric investigation of non-modal mechanisms at the leading edge of blunt bodies. Reynolds- and Mach-numbers trends associated with the perturbations optimally amplified by the flow were identified.

Optimal perturbations were obtained using resolvent analysis. To study a paraboloid body, a curvilinear grid formulation was implemented in a linear stability code. The baseflow used for analysis was obtained by time marching the non-linear flow equations.

Close to the stagnation point, maximum perturbation amplification occurs for zero-frequency disturbances, indicating the potential role of low-frequency disturbances. Optimal forcing and response modes indicate a receptivity mechanism associated with free-stream vorticity that enters the boundary layer near the stagnation point and then exploits the lift-up effect to create streaky structures at the body surface.

In the incompressible regime, a parametric investigation reveals that for increasing Reynolds number, i.e., increasing bluntness, the maximum amplification factor increases with $Re^{1/2}$. At higher Mach numbers, compressibility effects were seen to increase the amplification further. A 20% increase in gain was observed between the incompressible and $Ma = 1.2$ regimes. Potentially more importantly, the results show a trend suggesting that compressibility effects sharply increase with Ma. The authors thus believe that further studies on this trend, increasing the range of Mach numbers investigated, may provide important insights for understanding the transition reversal observed in hypersonic blunt bodies [27]. These trends reinforce the importance of non-modal mechanisms for blunt bodies at high Reynolds numbers in the incompressible and compressible limits.

The results complement previous receptivity studies. The trends presented are consistent with the switch from modal to non-modal transition mechanisms in hypersonic flows around blunt bodies [27]. In the low Mach regime, the decreasing receptivity of Tollmien-Schlichting waves with bluntness [11] points towards a similar phenomenon in incompressible flow: as bluntness increases, the role of non-modal mechanisms tends to overcome that of modal mechanisms, potentially leading to a transition to turbulent close to the stagnation point.

Finally, the linear mechanism by which free-stream disturbances penetrate the boundary layer complements previously studied transition routes for flow over a flat plate. While for moderate free-stream disturbances in the incompressible limit, non-linear receptivity is the dominant mechanism by which perturbations enter the boundary layer Brandt et al [2], a linear receptivity mechanism tends to dominate at lower turbulence intensities. We have thus studied one such mechanism: the ingestion of vortical disturbances at the stagnation point.

The trends obtained here are consistent with previous studies on the blunt-body paradox in hypersonic conditions. The paradox comes from observations that, in hypersonic flows, the transition points move downstream with increasing bluntness up to a critical bluntness, after which it quickly moves upstream. Although limited to low Mach numbers, the amplification trends with Reynolds number presented in this work are consistent with non-modal mechanisms underpinning the transition reversal. A follow-up study will extend the trend observed here to higher Mach numbers.

Funding This work is part of the project TRANSITION supported by Région Nouvelle-Aquitaine under grant 2018-1R10220. This work has been granted access to the HPC resources of IDRIS under the allocations A0092A10868 and A0112A10868 made by GENCI (Grand Equipement National de Calcul Scientifique).

Author contributions E.M. wrote the manuscript and prepared the figures. E.M. and O.S developed the code used in the analysis. C.C. provided the baseflow used in the study. E.M. G.L. and P.J. interpreted the results and investigated the physical mechanisms at play.

Data availability No datasets were generated or analysed during the current study.

Declarations

Conflict of interest The authors declare no competing interests.

Ethical approval Not applicable.

References

1. Andersson, P., Berggren, M., Henningson, D.S.: Optimal disturbances and bypass transition in boundary layers. Phys. Fluids **11**(1), 134–150 (1999). https://doi.org/10.1063/1.869908
2. Brandt, L., Schlatter, P., Henningson, D.S.: Transition in boundary layers subject to free-stream turbulence. J. Fluid Mech. **517**, 167–198 (2004). https://doi.org/10.1017/S0022112004000941
3. Buter, T.A., Reed, H.L.: Boundary layer receptivity to free-stream vorticity. Phys. Fluids **6**(10), 3368–3379 (1994)
4. Chu, B.T.: On the energy transfer to small disturbances in fluid flow (Part I). Acta Mech. **1**(3), 215–234 (1965)
5. Edgington-Mitchell, D., Wang, T., Nogueira, P., et al.: Waves in screeching jets. J. Fluid Mech. **913**, A7 (2021). https://doi.org/10.1017/jfm.2020.1175
6. Farghadan, A., Towne, A., Martini, E., et al.: A randomized time-domain algorithm for efficiently computing resolvent modes. In: AIAA Paper. American Institute of Aeronautics and Astronautics, pp. 2021–2896 (2021). https://doi.org/10.2514/6.2021-2896
7. Fedorov, A., Tumin, A.: Evolution of disturbances in entropy layer on blunted plate in supersonic flow. AIAA J. **42**(1), 89–94 (2004). https://doi.org/10.2514/1.9033
8. Fischer, PF., Patera. AT.: Parallel spectral element methods for the incompressible Navier-Stokes equations. In: Solution of superlarge problems in computational mechanics, pp. 49–65. Springer (1989)
9. Goldstein, M.E.: Scattering of acoustic waves into Tollmien–Schlichting waves by small streamwise variations in surface geometry. J. Fluid Mech. **154**, 509–529 (1985). https://doi.org/10.1017/S0022112085001641
10. Gómez, F., Blackburn, H.M., Rudman, M., et al.: A reduced-order model of three-dimensional unsteady flow in a cavity based on the resolvent operator. J. Fluid Mech. **798**, R2 (2016). https://doi.org/10.1017/jfm.2016.339
11. Haddad, O.M., Corke, T.C.: Boundary layer receptivity to free-stream sound on parabolic bodies. J. Fluid Mech. **368**, 1–26 (1998). https://doi.org/10.1017/S0022112098001311
12. Hanifi, A., Schmid, P.J., Henningson, D.S.: Transient growth in compressible boundary layer flow. Phys. Fluids **8**(3), 826–837 (1996). https://doi.org/10.1063/1.868864
13. Homann, F.: Einfluß großer zähigkeit bei strömung um zylinder. Forschung auf dem Gebiet des Ingenieurwesens A **7**(1), 1–10 (1936)
14. Kamal, O., Lakebrink, M.T., Colonius, T.: Global receptivity analysis: physically realizable input–output analysis. J. Fluid Mech. **956**, R5 (2023). https://doi.org/10.1017/jfm.2023.48
15. Lin, N., Reed, H.L., Saric, W.S.: Effect of Leading-edge geometry on boundary-layer receptivity to freestream sound. In: Hussaini, M.Y., Kumar, A., Streett, C.L. (eds.) Instability, Transition, and Turbulence, pp. 421–440. Springer, New York, NY (1992)
16. Lin, R.S., Malik, M.R.: On the stability of attachment-line boundary layers. Part 1. The incompressible swept Hiemenz flow. J. Fluid Mech. **311**, 239–255 (1996)
17. Lin, R.S., Malik, M.R.: On the stability of attachment-line boundary layers. Part 2. The effect of leading-edge curvature. J. Fluid Mech. **333**, 125–137 (1997)
18. Luchini, P.: Reynolds-number-independent instability of the boundary layer over a flat surface: Optimal perturbations. J. Fluid Mech. **404**, 289–309 (2000). https://doi.org/10.1017/S0022112099007259
19. Mack, C., Schmid, P.J.: Global stability of swept flow around a parabolic body: Features of the global spectrum. J. Fluid Mech. **669**, 375–396 (2011). https://doi.org/10.1017/S0022112010005252
20. Mack, LM.: (1965) The stability of the compressible laminar boundary layer according to a direct numerical solution(Stability of compressible laminar boundary layer according to direct numerical solution), pp. 329–362 (1965)
21. Martini, E., Rodríguez, D., Towne, A., et al.: Efficient computation of global resolvent modes. J. Fluid Mech. **919**, A3 (2021). https://doi.org/10.1017/jfm.2021.364
22. Meneghello, G., Schmid, P.J., Huerre, P.: Receptivity and sensitivity of the leading-edge boundary layer of a swept wing. J. Fluid Mech. **775**, R1 (2015). https://doi.org/10.1017/jfm.2015.282
23. Monokrousos, A., Åkervik, E., Brandt, L., et al.: Global three-dimensional optimal disturbances in the Blasius boundary-layer flow using time-steppers. J. Fluid Mech. **650**, 181–214 (2010). https://doi.org/10.1017/S0022112009993703
24. Morkovin, MV.: (1969) On the many faces of transition. In: Wells, C.S. (ed.) Viscous Drag Reduction, pp. 1–31. Springer, Boston, MA. https://doi.org/10.1007/978-1-4899-5579-1_1
25. Nogueira, P.A.S., Cavalieri, A.V., Hanifi, A., et al.: Resolvent analysis in unbounded flows: Role of free-stream modes. Theoretical and Computational Fluid Dynamics, pp. 1–14 (2020). https://doi.org/10.1007/s00162-020-00519-x
26. Obrist, D., Schmid, P.J.: On the linear stability of swept attachment-line boundary layer flow. Part 2. Non-modal effects and receptivity. J. Fluid Mech. **493**, 31–58 (2003). https://doi.org/10.1017/S0022112003005780
27. Paredes, P., Choudhari, M.M., Li, F.: Blunt-body paradox and transient growth on a hypersonic spherical forebody. Phys. Rev. Fluids **2**(5), 053903 (2017). https://doi.org/10.1103/PhysRevFluids.2.053903
28. Paredes, P., Choudhari, M.M., Li, F.: Mechanism for frustum transition over blunt cones at hypersonic speeds. J. Fluid Mech. **894**, A22 (2020). https://doi.org/10.1017/jfm.2020.261
29. Schmid, P.J., Henningson, D.S.: Stability and Transition in Shear Flows, vol 142. Springer (2012)
30. Schmidt, O.T., Rist, U.: Linear stability of compressible flow in a streamwise corner. J. Fluid Mech. **688**, 569–590 (2011). https://doi.org/10.1017/jfm.2011.405
31. Schmidt, O.T., Rist, U.: Viscid-inviscid pseudo-resonance in streamwise corner flow. J. Fluid Mech. **743**, 327–357 (2014). https://doi.org/10.1017/jfm.2014.31
32. Schmidt, O.T., Towne, A., Rigas, G., et al.: Spectral analysis of jet turbulence. J. Fluid Mech. **855**, 953–982 (2018). https://doi.org/10.1017/jfm.2018.675
33. Shahriari, N., Bodony, D.J., Hanifi, A., et al.: Acoustic receptivity simulations of flow past a flat plate with elliptic leading edge. J. Fluid Mech. **800**, R2 (2016). https://doi.org/10.1017/jfm.2016.433
34. Tam, C.K.W.: Excitation of instability waves in a two-dimensional shear layer by sound. J. Fluid Mech. **89**(2), 357–371 (1978). https://doi.org/10.1017/S0022112078002645

35. Towne, A., Rigas, G., Kamal, O., et al.: Efficient global resolvent analysis via the one-way Navier-Stokes equations. J. Fluid Mech. **948**, A9 (2022). https://doi.org/10.1017/jfm.2022.647
36. Tumin, A., Reshotko, E.: Spatial theory of optimal disturbances in boundary layers. Phys. Fluids **13**(7), 2097–2104 (2001). https://doi.org/10.1063/1.1378070
37. Wanderley, J.B.V., Corke, T.C.: Boundary layer receptivity to free-stream sound on elliptic leading edges of flat plates. J. Fluid Mech. **429**, 1–21 (2001). https://doi.org/10.1017/S0022112000002548
38. Wang, C., Lesshafft, L., Cavalieri, A.V.G., et al.: The effect of streaks on the instability of jets. J. Fluid Mech. **910**, A14 (2021). https://doi.org/10.1017/jfm.2020.963
39. Weidman, P.D.: Non-axisymmetric Homann stagnation-point flows. J. Fluid Mech. **702**, 460–469 (2012). https://doi.org/10.1017/jfm.2012.197